Fixed grid numerical modelling of frost growth and densification

Eduard Bartrons[a,b,*], Pedro Galione[c], Carlos David Pérez-Segarra[a,**]

[a] *Heat and Mass Transfer Technological Center, Universitat Politècnica de Catalunya, Carrer de Colom 11, 08222 Terrassa (Barcelona), Spain*
[b] *Termo Fluids, S.L., Av. Jacquard 97 1-E, 08222 Terrassa (Barcelona), Spain*
[c] *Instituto de Ingeniería Mecánica y de Producción Industrial (IIMPI), Universidad de la República (UdelaR), 11300 Montevideo, Uruguay*

Abstract

A fixed-grid-porous-media method capable of simulating the growth and densification of frost sheets is here presented. A velocity field is calculated across the entire domain, in which a porous media treatment is given to the ice-containing cells. The transported temperature and vapour density are used to define the thermophysical state of each cell, which might enable phase change. As an improvement to Bartrons *et al.*, 2017, the method hereby presented accounts for solidification and sublimation phase transitions. The explicit time step has also been increased by using a semi-implicit treatment of the energy equation. Furthermore, a special boundary condition for cold surfaces has been developed in order to overcome the averaging effect that prevents ice formation in the cells adjacent to the wall. The method is then tested with a study case of a duct flow with a non-homogeneously cooled lower boundary. Several numerical tests are carried out in order to understand the capabilities of the model. The influence of accounting for the convection, as well as the enhanced diffusion resistance factors within the frost layer, is studied by means of the calculated porosity and velocity fields throughout the domain.

Keywords: Frost growth, Frost densification, Fixed grid, Numerical model, Porous media

Nomenclature

c_p	specific heat capacity, J/(kgK)
C	Darcian source term constant, kg/(m^{3}s)
D	diffusivity, m^2/s

*Eduard Bartrons
**Carlos David Pérez-Segarra
Email addresses: eduard@cttc.upc.edu (Eduard Bartrons), pgalione@fing.edu.uy (Pedro Galione), cttc@cttc.upc.edu (Carlos David Pérez-Segarra)

h enthalpy, J/kg
p pressure, Pa
S Darcian source term coefficient, kg/(m^{3}s)
T temperature, K
u averaged or seepage (Darcy) velocity $\varepsilon_v \cdot v$, m/s
v velocity, m/s
V volume, m^3
Y_v water vapour concentration, $\mathrm{kg_v/kg_{ha}}$

Greek symbols
ε porosity
λ conductivity, W/mK
μ diffusion resistance factor
μ_{ha} dynamic viscosity, kg/(m s)
ρ density, kg/m^3
τ tortuosity
$\dot{\omega}_i$ ice generation, kg/(m^{3}s)
$\dot{\omega}_v$ water vapour generation, kg/(m^{3}s)

Subscript
v water vapour
da dry air
ha humid air
i ice
fl frost layer (contains ice and humid air)
m mixture: can correspond to fl ($\varepsilon \neq 1$) or ha ($\varepsilon = 1$)
sat saturated
in inlet

Superscript
n current time step

1. Introduction

The formation of frost is a common phenomenon in nature that involves growth of ice crystals on cold surfaces. The build-up of such porous structures causes malfunctioning in a wide variety of industrial applications, i.e. power transmission line systems, refrigerators and heat exchangers among others. In wind turbines, frost adhesion may be strong under low speed winds [1]. Deicing liquids are often used to remove the nocturnal frost generated on aircraft wings, which adds weight and reduces the aerodynamical performance. Recent studies suggest that frost can also form on aircraft wings during in-flight when crossing supersaturated icing clouds [2]. Hence, providing robust numerical methods to predict the appearance and growth of frost is of key importance to counteract such undesired effects and, as a consequence, improving designs that enhance safety, increase efficiency and avoid mechanical damage.

The incipient stages of frost formation, triggered by either desublimation or condensation frosting [3], range from an initial heterogeneous nucleation at a surface, until a network of inter-connected frozen droplets is formed. This provides the foundation upon which out-of-plane frost growth can happen. A comprehensive number of studies have modelled the latter from a macroscopical point of view. Based on how equations are set, frost growth models coupled with a free air flow region, using a finite volume approach, can be divided into two main blocks: the two-domain approach and the single-domain approach.

The two-domain approach consists in solving separately the frost and the free air regions. If the implemented frost growth model is 1D (see [4, 5, 6, 7, 8, 9] among others), a mesh accounting for the frost domain is not specifically needed [10]. Moreover, it allows implementing a frost growth model with a zero frost thickness initial condition [9]. On the other hand, 2D and 3D frost growth models need a mesh to account for the frost domain, where distributions of the porosity, or the frost density, and the temperature are calculated. These models do need an initial frost thickness [11, 12, 13, 14], as the mesh occupies a certain amount of volume. Despite the fact that the results for frost growth remain unaffected when using close to zero initial thicknesses [15], the region where frost will grow must be known in advance. Regardless of the implemented frosting model, either static or dynamic meshes can be used. The first is more common in the literature, despite its inherent lack of accuracy when tracking the frost-air interface [11, 10, 12]. When dynamic meshes are used, an ALE formulation is set to correct the mass and energy fluxes due to the imposed grid deformations derived from the frost growth [16, 17, 18, 19]. The two domains are then coupled by means of a mass and energy balance at the frost-air interface along with a water vapour pressure condition.

There are just a few studies using single-domain approaches (see [20, 21, 22]). These do not need an initial frost thickness, fact that not only allows solving the appearance of frost, but also having several unconnected frost regions growing simultaneously. Similarly to the two-domain approach with a static mesh, the usage of fixed grids compared to deformable grids could dramatically reduce the simulation computational costs and resources, as the mesh does not need to readapt at each iteration. Furthermore, no extra communication between the two domains is required.

The present paper sets a single-domain approach method, as an improvement to [23]. The new model, which consists of a single set of equations, accounts for the formation and sublimation of frost by means of a momentum equation for flow through the frost layer (based on the previous works of Galione *et al.* [24, 25], in the line of the works of Hsu and Cheng [26] and Voller and Prakash [27]), as well as a water vapour transport and energy equations that determine the state of a cell, and thus, the phase change. An effort has been put towards maximizing the explicit time step, by evaluating the diffusive term of the energy equation implicitly. Moreover, in order to ensure ice generation close to cold surfaces, a special treatment to such boundaries is here presented.

The proposed model is then used for simulating the case of a duct flow with a non-homogeneously cooled lower surface carried out by Kwon *et al.* [28]. Several

numerical tests are conducted with the aim of understanding the capabilities of the model. In particular, the impact to the frost growth when using different porous media treatment, as well as the usage of diffusion resistance factors above 1 is here analysed. Furthermore, a qualitative study of the convective effects within the frost sheet is also discussed.

2. Mathematical model

The present analysis assumes that: (a) water vapour, dry air and ice inside the frost layer are in local thermal equilibrium, i.e., $T_{\mathrm{ha}} = T_v = T_{\mathrm{da}} = T_i$; (b) water vapour inside the frost layer is saturated, (c) no movement of the ice crystals is allowed ($\vec{u}_i = 0$), and (d) temporal variation of the mixture density is neglected when calculating the velocity field.

The local volume averaging technique is used, where ε_v represents the volumetric vapour or humid air fraction, which can take values between 0 (ice) and 1 (humid air). The equalty $\varepsilon_v + \varepsilon_i = 1$ must be preserved.

Based on the above-mentioned hypotheses, the resulting governing equations for incompressible flow (global mass, momentum, water vapour transport and energy) are:

$$\cancelto{0}{\frac{\partial \rho_m}{\partial t}} + \nabla \cdot (\rho_{\mathrm{ha}} \vec{u}) = 0 \tag{1}$$

$$\begin{aligned} \frac{\partial}{\partial t}(\rho_{\mathrm{ha}}\vec{u}) + \nabla \cdot \left(\rho_{\mathrm{ha}} \frac{\vec{u} \otimes \vec{u}}{\Xi}\right) = &- \nabla p + \nabla \cdot \left[\mu_{\mathrm{ha}} \left(\nabla \vec{u} + (\nabla \vec{u})^T\right)\right] \\ &- \frac{2}{3} \nabla \mu \, (\nabla \cdot \vec{u}) + \rho_{\mathrm{ha}} \varepsilon_v \vec{g} - S\vec{u} \end{aligned} \tag{2}$$

$$\frac{\partial}{\partial t}(\varepsilon_v \rho_v) + \nabla \cdot (\rho_v \vec{u}) = \nabla \cdot (\rho_{\mathrm{ha}} \mu D_v \nabla Y_v) + \dot{\omega}_v \tag{3}$$

$$\frac{\partial}{\partial t}(\rho_m h_m) + \nabla \cdot (\rho_{\mathrm{ha}} h_{\mathrm{ha}} \vec{u}) = \nabla \cdot (\lambda_m \nabla T) + \nabla \cdot \left[(h_v - h_{\mathrm{da}}) \, \rho_{ha} \mu D_v \nabla Y_v\right] \tag{4}$$

where:

$$\rho_m = \varepsilon_v \rho_{\mathrm{ha}} + (1 - \varepsilon_v)\rho_i \tag{5}$$

$$\rho_m h_m = \varepsilon_v \rho_{\mathrm{ha}} h_{\mathrm{ha}} + (1 - \varepsilon_v)\rho_i h_i \tag{6}$$

$$\rho_{\mathrm{ha}} = \rho_v + \rho_{\mathrm{da}} \tag{7}$$

Equation 2 corresponds to the momentum equation for flow through a porous medium, where only the Darcian source term, $S\vec{u}$, has been preserved, accounting for the drag force produced by the solid to the fluid flow.

The present study analyzes two forms of the momentum equation:

a) The simplified model for mushy regions put forward by Voller and Prakash[27], where $\Xi = 1$ and $S = S_{\mathrm{VP}}$.

b) The porous media model put forward by Hsu and Cheng[26], where $\Xi = \varepsilon_v$ and $S = S_{\mathrm{HC}}$.

Author	Diffusion resistance factor
Prager *et al.* [31]	$\mu = 0.5\varepsilon_v\left(1+\varepsilon_v\right)$
Le Gall *et al.* [17]	$\mu = \varepsilon_v/\left(1-0.58\left(1-\varepsilon_v\right)\right) + F10\left(1-\varepsilon_v\right)\varepsilon_v^{10}$

Table 1: Implemented correlations of the diffusion resistance factor.

The selected correlations for the coefficient S are treated in detail in Section 3.1.1.

The water vapour transport and energy equations deduced in [19, 29] are here extended to account for the advective terms. Observe that these terms, which appear in Eqs. 1-4, contain uniquely the transport of the humid air properties, as the ice phase is assumed to be motionless [24].

The source term $\dot{\omega}_v$ that appears in Eq. 3 represents the generation or destruction of water vapour. This value is equally opposite to the generation or destruction of the ice phase, $\dot{\omega}_i$. Hence,

$$\dot{\omega}_v = -\dot{\omega}_i = -\frac{\partial(\varepsilon_i \rho_i)}{\partial t} \tag{8}$$

The diffusion resistance factor μ (not to be confused with the dynamic viscosity μ_{ha} in the momentum equation), commonly defined in non-reactive porous media as $\mu \equiv \varepsilon_v \tau$, is a measure of the added difficulty of the water vapour to flow through the ice crystal pores. However, the former definition does not entirely apply for frost, since an effective mass diffusion is allowed between ice shelves due to temperature gradients ($\mu \neq 0$ in a humid air-ice series arrangement, see Auracher [30]). The correlations used in this paper, shown in Table 1 and in Fig. 1 for different values of ε_v, are the ones proposed by Prager *et al.* [31] and Le Gall *et al.* [17].

On the other hand, the thermal conductivity of the mixture, λ_m, is defined either by means of the Studnikov expression[32] in the humid air region, or by the empirical correlation proposed by Na and Webb[6] within the frost layer. The latter reads as:

$$\lambda_{\mathrm{fl}} = \xi \lambda_{\mathrm{par}} + (1-\xi)\,\lambda_{\mathrm{ser}} \tag{9}$$

where:

$$\lambda_{\mathrm{par}} = \left(1 - \frac{\rho_{\mathrm{fl}}}{\rho_i}\right)\lambda_{\mathrm{ha}} + \frac{\rho_{\mathrm{fl}}}{\rho_i}\lambda_i$$

$$\lambda_{\mathrm{ser}} = \left[\frac{\rho_{\mathrm{fl}}}{\rho_i}\frac{1}{\lambda_i} + \left(1 - \frac{\rho_{\mathrm{fl}}}{\rho_i}\right)\frac{1}{\lambda_{\mathrm{ha}}}\right]^{-1}$$

And the modeled ξ parameter is given in Table 2.

The air is treated as a semi-perfect gas. The reader is referred to [19] for a further description of the implemented correlations of the thermo-physical properties of the model.

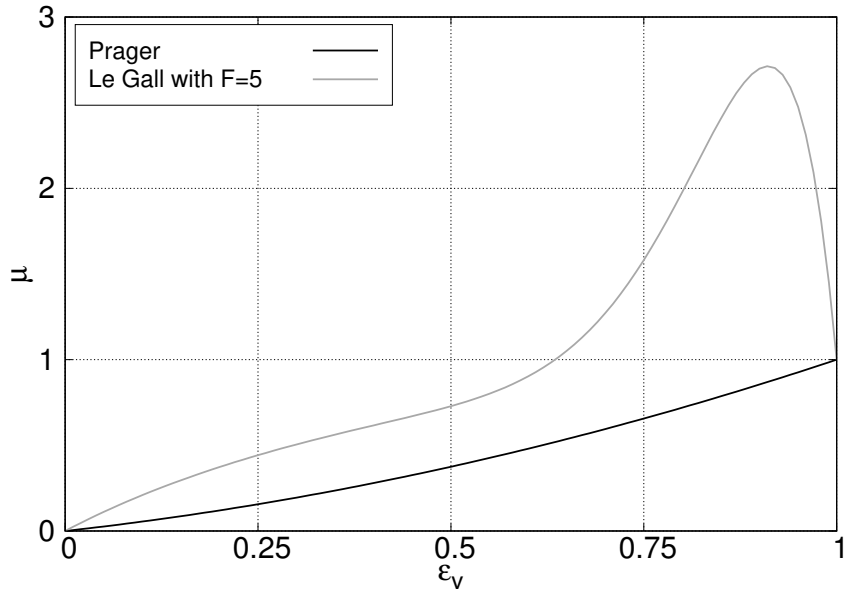

Figure 1: Tested diffusion resistance factor correlations. Le Gall *et al.* [17] with and F factor of 5, and the widely used correlation from Prager *et al.* [31].

	Range	ξ
(i)	$-10 < T_w < -4 \ \ ^\circ\mathrm{C}$	$0.283 + e^{-0.020\rho_{\mathrm{fl}}}$
(ii)	$-21 < T_w < -10 \ ^\circ\mathrm{C}$	$0.140 + 0.919e^{-0.0142\rho_{\mathrm{fl}}}$
(iii)	$T_w < -21 \ ^\circ\mathrm{C}$ and $\rho_{\mathrm{fl}} < 200\mathrm{kg/m^3}$	$0.0107 + 0.419e^{-0.00424\rho_{\mathrm{fl}}}$
(iv)	$T_w < -21 \ ^\circ\mathrm{C}$ and $\rho_{\mathrm{fl}} > 200\mathrm{kg/m^3}$	$0.005\rho_{\mathrm{fl}}\left(0.0107 + 0.419e^{-0.00424\rho_{\mathrm{fl}}}\right)$

Table 2: ξ parameter of Na and Webb's effective thermal conductivity correlation.

3. Numerical implementation

The mathematical model is implemented into an in-house C++ computer code called TermoFluids. The reader is referred to [33] for details on the TermoFluids framework that are beyond the scope of this paper. A finite volume approach and a collocated discretization is used along with explicit time integration schemes. In particular, the time integration scheme corresponds to the 2^{nd} order explicit Linear Multi-step method (k2LM), in which the time step is dynamically adapted by estimating the upper bounds of the eigenvalues of the convective and the diffusive operators [34].

3.1. Mass and momentum

The velocities induced as a result of the density changes (mainly given by phase changes) can be neglected when comparing them to the resulting velocity field of forced convection driven flows. As a consequence, the transient term of the continuity equation (Eq. 1) is neglected, as formerly stated by assumption (d). Moreover, due to the fact that the gravitational effects of the problem of study are negligible, the buoyancy term of Eq. 2 is also neglected. The resulting time-discretization of the Eqs.1 and 2 is:

$$\nabla \cdot \left(\rho_{\mathrm{ha}} \vec{u}\right)^{n+1} = 0 \tag{10}$$

$$\frac{\left(\rho_{\mathrm{ha}} \vec{u}\right)^{n+1} - \left(\rho_{\mathrm{ha}} \vec{u}\right)^{n}}{\Delta t} = R^{n+\alpha}\left(\vec{u}\right) - \nabla p^{n+1} - S\vec{u}^{n+1} \tag{11}$$

where $R^{n+\alpha}$ represents the sum of the convective and diffusive terms integrated between time steps n and $n+1$ using some integration scheme (in this case, the above mentioned k2LM). The momentum source term is treated implicitly due to stability reasons [24].

Decoupling of $\vec{u}^{n+1}$ and p^{n+1} is carried out applying divergence, imposing mass conservation (Eq. 10) and rearranging terms:

$$\Delta t \nabla \cdot \left(\frac{\nabla p^{n+1}}{1 + \Delta t S/\rho_{\mathrm{ha}}}\right) = \nabla \cdot \left(\frac{\rho_{\mathrm{ha}} u^{p}}{1 + \Delta t S/\rho_{\mathrm{ha}}}\right) \tag{12}$$

where

$$\rho_{\mathrm{ha}} \vec{u}^{p} = \rho_{\mathrm{ha}} \vec{u}^{n} + \Delta t R^{n+\alpha} \tag{13}$$

is a pseudo-predictor velocity. And thus:

$$\left(\rho_{\mathrm{ha}} \vec{u}\right)^{n+1} = \left(\frac{\rho_{\mathrm{ha}} \vec{u}^{p} + \Delta t \nabla p^{n+1}}{1 + \Delta t S/\rho_{\mathrm{ha}}}\right) \tag{14}$$

from where the new velocity field ($\vec{u}^{n+1}$) is calculated, and where $1/\left(1 + \Delta t S/\rho_{\mathrm{ha}}\right)$ acts as a damping factor of the velocity. The density ρ_{ha} is evaluated at time n because the momentum equation is not iterated with the energy and vapour transport equations. A detailed explanation of the procedure is given in [24, 25].

3.1.1. Darcian source term coefficient (S)

The coefficient S can take various forms. In particular, the present study uses two of them. Whenever using the model put forward by Voller and Prakash [27], the following expression is used:

$$S_{\mathrm{VP}} = C_{\mathrm{VP}} \frac{(1-\varepsilon_v)^2}{\varepsilon_v^3 + q} \tag{15}$$

where C_{VP} is an arbitrary constant and q is a very small value included to avoid division by zero (when $\varepsilon_v \to 0$, S_{VP} increases and consequently, convection is strongly reduced).

When the momentum equation corresponds to the one proposed by Hsu and Cheng [26], the preferred expression, deduced from Kozeny-Carman equation, reads as:

$$S_{\mathrm{HC}} = \frac{150}{(\psi d_p)^2} \frac{\mu_{\mathrm{ha}}(1-\varepsilon_v)^2}{\varepsilon_v^2} \tag{16}$$

Where ψ is the sphericity of the packed bed particles, and d_p the particle diameter. These two values will evidently not be constant throughout the frost layer. Therefore, an expression for d_p, probably depending on ε_v, should be determined in order to accurately simulate the phase change within the frost layer. Due to the fact that such correlation is not available, some arbitrary values are hereby tested using the constant C_{HC}, defined as:

$$C_{\mathrm{HC}} \equiv \frac{150}{(\psi d_p)^2} \tag{17}$$

The two values used for C_{HC} are set so the resulting damping curves are the most similar to the ones using the tested values of C_{VP}.

As previously stated in Eq. 11, the Darcian source term is treated implicitly, from which the coefficient S contributes on the dampening of the velocity through the previously named damping factor. Fig. 2 shows the damping produced for different values of C. The results obtained using these values are compared and discussed in Sec. 5.

3.2. Water vapour transport

Expressing Eq. 3 in a non-conservative form for ρ_v:

$$\varepsilon_v \frac{\partial \rho_v}{\partial t} + \nabla \cdot (\rho_v \vec{u}) = \nabla \cdot (\rho_{\mathrm{ha}} \mu D_v \nabla Y_v) + (\rho_i - \rho_v) \frac{\partial \varepsilon_v}{\partial t} \tag{18}$$

It can be seen that the transient source term containing the derivative of the porosity could give stability problems due to the fact that the error in the solution of ρ_v caused by assuming the vapour fraction derivative would grow significantly. Indeed,

$$\frac{\Delta \rho_v}{\rho_v} \propto \left(\frac{\rho_i}{\rho_v} - 1 \right) \frac{\Delta \varepsilon_v}{\varepsilon_v} \tag{19}$$

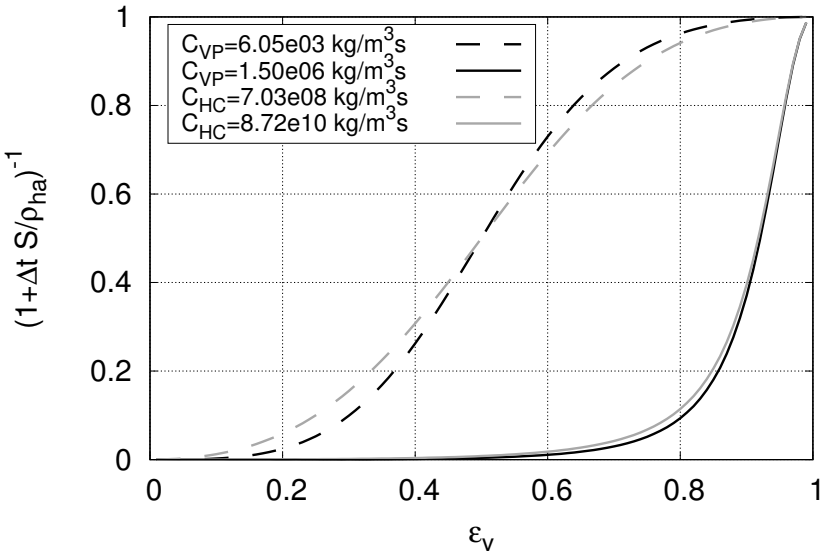

Figure 2: Damping factor vs. ε_v for various values of C. Values of $C_{\mathrm{VP}} = 6.05e03$ kg/m^{3}s and $C_{\mathrm{HC}} = 7.03e08$ kg/m^{3}s have been taken such that the damping factor is 0.5 when $\varepsilon_v = 0.5$.

from which the factor $(\rho_i/\rho_v - 1)$ is of the order of 10^5. Hence, a small as 0.1 relative error in ε_v will induce an error in ρ_v of 10^4.

In order to overcome this numerical issue, Eq. 3 is separated into two equations: one for ρ_v, which corresponds to Eq. 18, and the other for ε_v defined hereafter.

$$(\rho_v - \rho_i)\frac{\partial \varepsilon_v}{\partial t} + \nabla \cdot (\rho_v \vec{u}) = \nabla \cdot (\rho_{\mathrm{ha}} \mu D_v \nabla Y_v) - \varepsilon_v \frac{\partial \rho_v}{\partial t} \tag{20}$$

Cells containing ice phase will compute ε_v from Eq. 20. Recall that the water vapour in cells with $\varepsilon_v \neq 1$ is under saturated conditions, from which ρ_v is directly calculated by means of the cell temperature. On the contrary, cells containing only humid air will compute ρ_v from Eq. 18.

Discretizing Eqs. 18 and 20 in time:

$$\rho_v^{n+1} = \rho_v^n + \frac{\Delta t}{\varepsilon_v^n}\Big[\underbrace{\nabla \cdot (\mu D_v \nabla \rho_v)}_{\mathcal{D}} - \underbrace{\nabla \cdot (\rho_v \vec{u})}_{\mathcal{C}}\Big]^{n+\alpha} - \underbrace{(\rho_v^n - \rho_i^n)\frac{\varepsilon_v^{n+1} - \varepsilon_v^n}{\Delta t}}_{\mathcal{S}} \tag{21}$$

$$\varepsilon_v^{n+1} = \varepsilon_v^n + \frac{\Delta t}{(\rho_v^n - \rho_i^n)}\Big[\underbrace{\nabla \cdot (\mu D_v \nabla \rho_v)}_{\mathcal{D}} - \underbrace{\nabla \cdot (\rho_v \vec{u})}_{\mathcal{C}}\Big]^{n+\alpha} - \underbrace{\varepsilon_v^n \frac{\rho_v^{n+1} - \rho_v^n}{\Delta t}}_{\mathcal{S}} \tag{22}$$

where $n + \alpha$ refers to the k2LM time integration scheme.

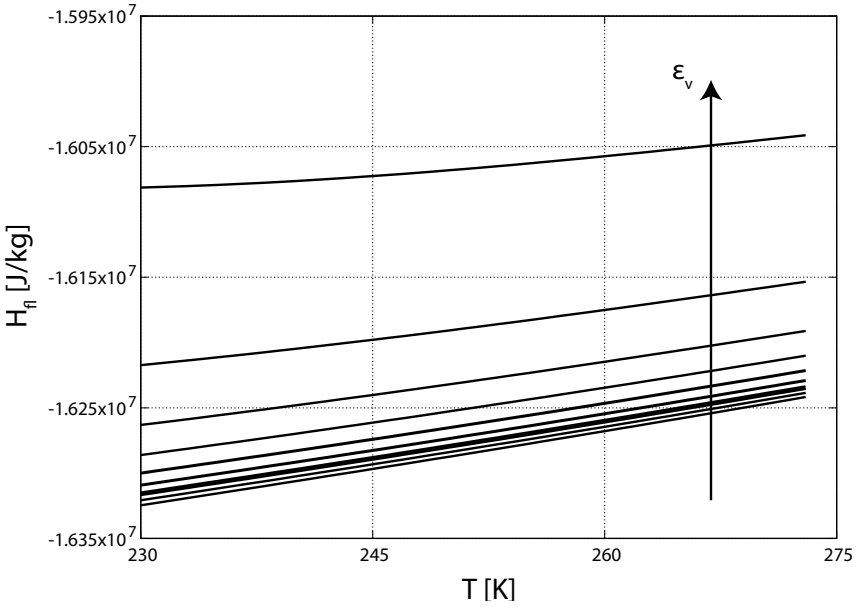

Figure 3: H-T dependance. Each curve is given at a fixed ε_v, from values of 0.1 to 0.9 with increments of 0.1.

A split method is implemented to solve the former. The method consists in solving the convective ($\mathcal{C}$) and diffusive ($\mathcal{D}$) terms explicitly, and once per time step, as shown in a simplified form in Eq.23.

$$\frac{\phi^* - \phi^n}{\Delta t} = -\mathcal{C}^n + \mathcal{D}^n \tag{23}$$

where ϕ stands for either ρ_v or ε_v. The source term ($\mathcal{S}$), on the contrary, is evaluated between time $n+1$ and n, and reconstructed at each iteration (see step 4 in Alg. 1, Sec. 3.4), as shown in Eq.24, to obtain ϕ^{n+1}.

$$\frac{\phi^{n+1} - \phi^*}{\Delta t} = -\mathcal{S}^{n+1} \tag{24}$$

3.3. Energy

The enthalpy-based energy equation given by Eq. 4 is rewritten in a non-conservative form in terms of the temperature. This change of the solving variable is preferred because of two main reasons: (a) isolating a temperature from Eq. 6 is not an easy task, and most important, (b) a small absolute error in the solution of the enthalpy translates into a big error in the temperature (see Fig. 3). The resulting energy equation is:

$$\rho_{\mathrm{fl}} c_{p,\mathrm{fl}} \frac{\partial T}{\partial t} + \nabla \cdot (\rho_{ha} h_{ha} \vec{u}) = \nabla \cdot (\lambda_m \nabla T) + \nabla \cdot \left[(h_v - h_{da}) \, \rho_{\mathrm{ha}} \mu D_v \nabla Y_v \right] \\ \cancel{-\varepsilon_v h_{\mathrm{ha}} \frac{\partial \rho_{\mathrm{ha}}}{\partial t}}^{\,0} - \rho_{\mathrm{ha}} \varepsilon_v (h_v - h_{\mathrm{da}}) \frac{\partial Y_v}{\partial t} - (\rho_{\mathrm{ha}} h_{\mathrm{ha}} - \rho_i h_i) \frac{\partial \varepsilon_v}{\partial t} \tag{25}$$

where the source term containing the humid air density derivative over time is neglected due to its very slow changes over time. The frost layer heat capacity, $c_{p,\mathrm{fl}}$, is defined as follows:

$$c_{p,\mathrm{fl}} = \frac{1}{\rho_{\mathrm{fl}}} \left[(1 - \varepsilon_v) \rho_i \bar{c}_{p,i} + \varepsilon_v \rho_{\mathrm{ha}} \bar{c}_{p,\mathrm{ha}} \right] \tag{26}$$

where $\bar{c}_{p,i}$ and $\bar{c}_{p,\mathrm{ha}}$ correspond to the averaged values of the specific heat capacity of ice and humid air, respectively.

The convective term is treated explicitly using the k2LM integration scheme. Moreover, due to the fact that the largest eigenvalue among the convective and diffusive terms of the full set of equations (Eqs. 2 - 4) corresponds to the diffusive term of the energy equation, it is hereby treated implicitly, resulting in an increase of the time step, and a reduction of the computational costs, compared to the ones reached in [23]. As a consequence, the limitation of the explicit time step is then given by the eigenvalue of the convective term of the momentum equation.

Because the problem of study imposes a temperature difference (not a water vapour concentration difference), and also the fact that it has been verified that the variations in time of the source term containing the concentration derivative ($\mathcal{S}_{12}$) are generally small, it is evaluated between time n and $n-1$. On the other hand, the source term containing the time derivative of the porosity is evaluated between time $n+1$ and n.

The discretized form of Eq. 25 is then:

$$T^{n+1} = T^n + \frac{\Delta t}{\left(\rho_{\mathrm{fl}} c_{p,\mathrm{fl}}\right)^n} \Bigg[\underbrace{- \nabla \cdot (\rho_{ha} h_{ha} \vec{u})^{n+\alpha}}_{\mathcal{C}} + \underbrace{\nabla \cdot (\lambda_m \nabla T_m)^{n+1}}_{\mathcal{D}} \\ + \underbrace{\nabla \cdot \left[(h_v - h_{da}) \, \rho_{\mathrm{ha}} \mu D_v \nabla Y_v \right]^n}_{\mathcal{S}_{11}} \underbrace{- \left[\rho_{\mathrm{ha}} \varepsilon_v \left(h_v - h_{\mathrm{da}} \right) \right]^n \frac{Y_v^n - Y_v^{n-1}}{\Delta t}}_{\mathcal{S}_{12}} \\ \underbrace{- \left(\rho_{\mathrm{ha}} h_{\mathrm{ha}} - \rho_i h_i \right)^n \frac{\varepsilon_v^{n+1} - \varepsilon_v^n}{\Delta t}}_{\mathcal{S}_2} \Bigg] \tag{27}$$

The steps of the implemented split method are detailed in Eqs. 28 and 29, in which the source term containing the derivative of the porosity, $\mathcal{S}_2$, is rebuilt at each iteration.

$$\frac{\phi^* - \phi^n}{\Delta t} = -\mathcal{C}^n + \mathcal{S}_{11}^n - \mathcal{S}_{12}^n \tag{28}$$

$$\frac{\phi^{n+1} - \phi^*}{\Delta t} = \mathcal{D}^{n+1} - \mathcal{S}_2^{n+1} \tag{29}$$

3.4. Methodology

The steps of the methodology are herewith summarized in Alg. 1. Due to the fact that most of the industrial applications that include frost growth involve forced convection driven flows, momentum is solved first (step 3) using the well known fractional step method[35]. Next, the transport of vapour (step 5) and the energy equations (step 6) are solved semi-implicitly throughout an iterative process in which the transient source terms are implicitly coupled and updated after each iteration (steps 4, 7 and 8). When the equations converge to a certain tolerance for variables ρ_v, ε_v and T, the calculation of the new time step is started.

The changes in the thermophysical state of a cell are regulated by the control variable `thStateChange`. This variable is set at each control volume, and it can take three values: 0 when there is no change of state (either if the cell remains as a frost cell or a humid air cell), 1 when the cell changes from a fully air containing cell to an ice containing cell, and 2 when the cell changes from a frost cell to a fully air containing cell.

Note that all cells begin with a `thStateChange` $= 0$. Some of them eventually meet the requirements to form ice, i.e. when the temperature of the cell is below the freezing point and the vapour density is larger than the saturation vapour density at the last calculated temperature. In this case, `thStateChange` is set to 1, fact that will let ε_v be calculated in the following iteration. Note that once an ε_v is calculated for a certain cell, its vapour density will be considered at saturation and thus, calculated by means of the new temperature. Moreover, the `thStateChange` will be reset to 0, and will remain 0 as long as that cell contains ice.

In the event that the new calculated temperature of an ice containing cell is higher than the freezing point, `thStateChange` is set to 2. The ice contained in it will sublimate, calculating ρ_v instead of ε_v in the next iteration.

As previously described, the method takes into account the solidification and the sublimation in the cells, but not the condensation nor the evaporation. Hence, the numerical experiments tested using this methodology must not meet those conditions that would trigger such phase transitions in the actual experiment. A graphical explanation of the limitations of the presented methodology is given in Fig. 4.

3.5. Special wall boundary condition

As previously discussed, the change of state of a cell occurs when the combination of the average temperature and vapour density values surpass the saturation curve (given that the temperature is below the freezing point). It is obvious that the amount of time needed by a fully humid-air-containing cell, neighbouring and ice-containing cell, to change its phase, will be directly related to the size of that cell. The smaller the cell is, the closer its temperature will be to that of its saturated neighbour, allowing an earlier generation of ice

Algorithm 1 Fixed grid - frost growth method

1: Initial conditions: `thStateChange` $= 0$

2: New time step Δt

3: Momentum equation

- Pseudo-predictor velocities u^p_{ha} using previous velocity fields (Eq. 13)
- Pressure eq.: calculation of coefs. and resolution using a linear solver to get p^{n+1} (Eq. 12)
- New velocity field u^{n+1}_{ha} using u^p_{ha} and p^{n+1} (Eq. 14)

4: New guessed values Φ^{n+1*}, where $\Phi = \{\rho_v, \varepsilon_v\}$ taken from last iteration

- Build transient source terms of Eqs. 21 , 22 and 27

5: Water vapour transport equations

if $\left[\left(\varepsilon_v^{n+1*} == 1\right)$ **and** $\left(\rho_v^{n+1} < \rho_{v,\text{ref,sat}}\right)$ **and** $\left(\texttt{thStateChange} == 0\right)\right]$ **or** $\left(\texttt{thStateChange} == 2\right)$ **then**

- Solve Eq. 21. Variable is vapour density: ρ_v^{n+1}
- `thStateChange` $= 0$

else *that is:* $\left(\varepsilon_v^{n+1*} \neq 1\right)$ ***or*** $\left(\rho_v^{n+1} \geq \rho_{v,\text{ref,sat}}\right)$ ***or*** $\left(\texttt{thStateChange} == 1\right)$

- Vapour is saturated. ρ_v will be calculated after calulating T^{n+1}
- Solve Eq. 22. Variable is vapour fraction: ε_v^{n+1}
- **if** $\left(\varepsilon_v^{n+1} < 1.0\right)$ **then** `thStateChange` $= 0$
- **else** $\varepsilon_v^{n+1} = 1.0$, `thStateChange` $= 2$
- **end if**

end if

6: Energy equation. Solve Eq. 27. Variable is temperature: T^{n+1}

- Calculate $\rho_{v,\text{sat}}(T^{n+1})$ from tables [36]

if $(T < 273.15K)$ **then** $\rho_{v,\text{ref,sat}} = \rho_{v,\text{sat}}$

else $\rho_{v,\text{ref,sat}} = r$, where r is a very big number to avoid passing a phase change condition when being at temperatures above freezing

end if

if $\left(\varepsilon_v^{n+1*} == 1\right)$ **and** $\left(\rho_v^{n+1} \geq \rho_{v,\text{ref}}\right)$ **and** $\left(\texttt{thStateChange} \neq 2\right)$ **then**

- `thStateChange` $= 1$
- $\rho_v = \rho_{v,\text{sat}}$

else if $\left(\varepsilon_v^{n+1*} < 1\right)$ **and** $(T < 273.15)$ **then**

- $\rho_v = \rho_{v,\text{sat}}$

else if $\left(\varepsilon_v^{n+1*} < 1\right)$ **and** $(T > 273.15)$ **then**

- `thStateChange` $= 2$
- $\varepsilon_v = 1$

end if

7: Update ρ_{ha} (in order to update such value, Y_v must also be updated)

8: **if** $|\varepsilon_v^{n+1} - \varepsilon_v^{n+1*}| > \delta$ **or** $|T^{n+1} - T^{n+1*}| > \delta$ **or** $|\rho_v^{n+1} - \rho_v^{n+1*}| > \delta$ **then**

- $\Phi^{n+1*} = \Phi^{n+1}$
- Go to 5

else

- Update (by order): ρ_{fl}, Y_v, thermophysical properties and h_{ha}
- Go to 2

end if

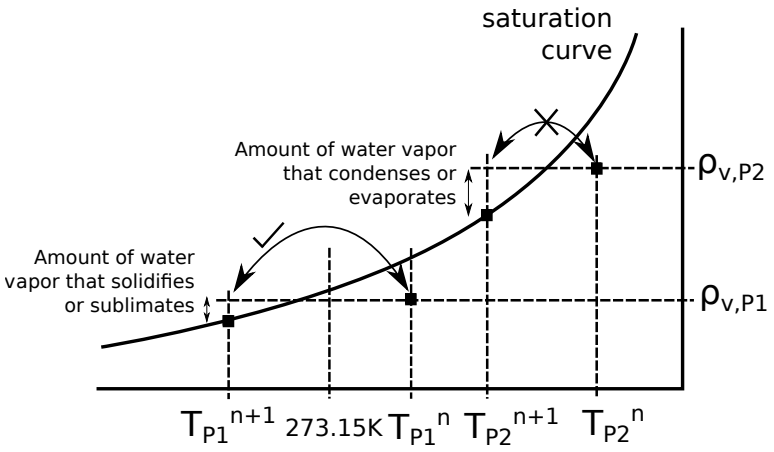

Figure 4: Capabilities and restrictions of the model. Possible phase change cases of a cell P1 solidifying or sublimating, and a cell P2 condensing or evaporating are here depicted.

in it. Note that the cell size dependency to the phase change will only affect the accuracy at which the frost-air interface is being tracked, but not necessarily the average growth velocity of the frost, which depends on the accuracy in the spatial representation of the relevant fields $(T, \rho_v, \varepsilon_v)$. Certainly, a larger size of a humid air cell will require its ice neighbouring cell to densify more before meeting the requirements to change its phase. However, once it becomes a frost cell, the space gained by the frost front will also be larger.

The former explanation is only valid if the domain already contains frost cells, as the latter densify and eventually let the neighbouring humid air cells change of phase. This section tackles the problem when still not having frost cells: depite that the conditions at the cold surface ensure the formation of ice at the wall, the humid air cells in which the cold surface is contained are big enough. Thus their average temperature never reduces to a point where phase change can happen. This lack of ice being formed in cells attached to the wall, and which would actually meet the conditions for frosting (only because of the wall temperature, not because of the average cell temperature), is the one attributed to the size of the mesh.

A solution to this instrinsic problem of finite volume approaches, while maintaining coarse-enough meshes, is addressed here by means of a boundary condition which allows the accumulation of water vapour at the wall in the form of ice. This ice is artificially accumulated at the wall until the summation of the density of water vapour at the cell node, and the one equivalent to the accumulated ice is larger than the saturated vapour density at the wall temperature, thus activating a phase change.

The algorithm associated to this boundary condition is presented in Alg. 2. In particular, when the temperature at the wall is below the dew and freezing points (see condition given in step 2 and shown in Fig. 5), ice should deposit on its surface. At this point, the vapour density zero derivative used as the default

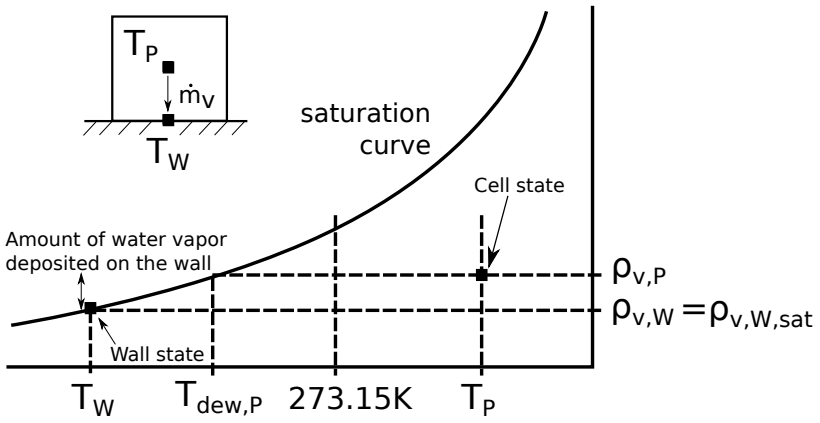

Figure 5: Conditions enabling phase change at the wall.

boundary condition is not applied.

The total deposited ice over a period of time reads as:

$$m_{i,\text{added}} = \int_0^t \dot{m}_v'' S dt \tag{30}$$

Where $\dot{m}_v''$ is the water vapour mass flux at the wall:

$$\dot{m}_v'' = D_v \nabla \rho_v \big|_W \hat{n}_W \tag{31}$$

The added mass of ice at the wall is stored as an equivalent water vapour volume fraction of the belonging cell:

$$\varepsilon_{v,W}' = \varepsilon_{v,W}' - V_{i,\text{added}}/V_{\text{cell}} \tag{32}$$

Where $V_{i,\text{added}} = m_{i,\text{added}}/\rho_i$. This volume fraction is then translated into an equivalent water vapour density, in step 4, as follows:

$$\rho_{v,\text{equiv}} = \rho_{v,P} + \rho_i \left(1 - \varepsilon_{v,W}'\right) \tag{33}$$

Where P stands for the cell central node. The cumulative value $\rho_{v,\text{equiv}}$ might eventually surpass the one from the saturation state at the averaged cell temperature (calculated in step 6 of Alg. 1). If the condition is satisfied, the cell state must change to frost. The variable `thStateChange` is then set to 1 in order to calculate ε_v in next iteration.

The implementation of this boundary condition is placed after step 6 of Alg. 1. The artificial variable ε_v' (not to be confused with ε_v) is only used for the purpose of this boundary condition. Moreover, once a cell starts being treated as a frost cell, this boundary condition is disapplied.

Algorithm 2 Boundary condition: vapour accumulation at the wall

1: Initial conditions: $\varepsilon'_v = 1$ (set along with `thStateChange` in step 1 of Alg. 1)
- Following steps placed after step 6 of Alg. 1

2: **if** $(T_W < T_{\text{dew},P})$ **and** $(T_W \leq 273.15K)$ **then** $\rho_{v,W} = \rho_{v,\text{sat}}\big|_{T_W}$ (see Fig.5)
else $\rho_{v,W} = \rho_{v,P}$ (see Fig.6)
end if

3: **if** $\left(\rho_{v,P} \neq \rho'_{v,W}\right)$ **then**
- $\dot{m}''_{i,\text{added}} = D_v \nabla\rho_v\big|_W \hat{n}_W$, where $\nabla\rho_v\big|_W \approx \left(\rho_{v,P} - \rho_{v,W}\right)/(\vec{d_{PW}} \cdot \hat{n}_W)$
- $V_{i,\text{added}} = \left(\dot{m}''_{i,\text{added}} S_W \Delta t\right)/\rho_i$
- $\varepsilon'_{v,W} = \varepsilon'_{v,W} - V_{i,\text{added}}/V_{\text{cell}}$
else $\varepsilon'_{v,W} = \varepsilon_{v,P}$
end if

4: **if** $\left(\varepsilon'_{v,W} \neq 1\right)$ **and** $(\varepsilon_{v,P} == 1)$ **then**
- $\rho_{v,\text{equiv}} = \rho_{v,P} + \rho_i\left(1 - \varepsilon'_{v,W}\right)$
if $\left(\rho_{v,\text{equiv}} > \rho_{v,sat}\big|_{T_P}\right)$ **then**
- `thStateChange` $= 1$
- $\rho_v^n = \rho_{v,\text{equiv}}$ and $\rho_v^{n+1*} = \rho_{v,\text{ref},P}$ when building the transient source terms in step 4 of Alg. 1
- $\varepsilon'_v = 1$
end if
end if

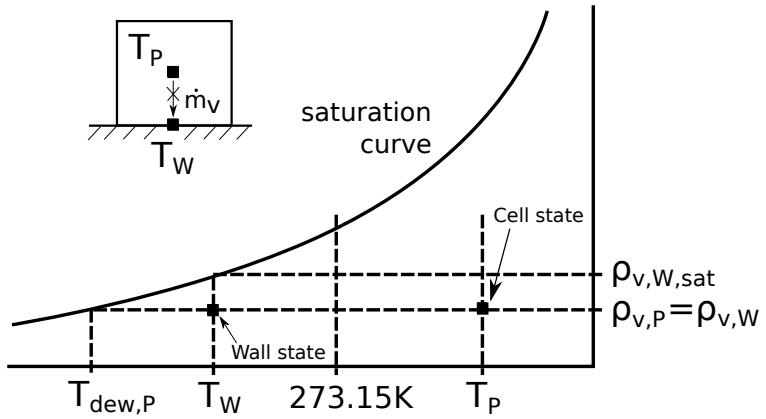

Figure 6: No phase change occurring at the wall.

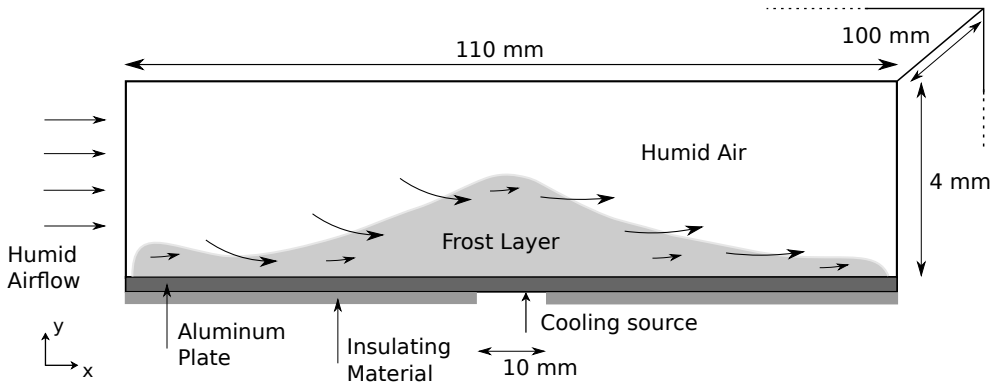

Figure 7: Detail of the test section used by Kwon *et al.* [28].

$T_{\mathrm{ha,in}}$ [K]	$v_{\mathrm{ha,in}}$ $[m/s]$	W_{in} $[kg_v/kg_{\mathrm{da}}]$	$T_W(x,t)$ [K]
275.15	1.5	0.00365	see Fig.8

Table 3: Experimental test conditions

4. Numerical experiment

The experimental case, carried out by Kwon *et al.* [28], consists of a duct flow with a rectangular cross section of 4 mm x 100 mm, and a total length of 110 mm. A cooling source of 10 mm wide is placed at the middle-length cross section of the test chamber, below the aluminum plate that constitutes the bottom side of the channel. Fig. 7 shows a detail of the test section. The tested experimental conditions are given in Table 3.

The total mass of frost was measured every 30 min, until 120 min. Frost thickness was also measured at 7 different locations along the test section. Measures were taken every 30 min, to the end of the experimental test (180 min).

The wall temperature, shown in Fig. 8, was monitored at 17 different positions at 5, 10, 15, 30, 60, 90, 120, 150 and 180 minutes. In order to take into account the temperature variations at the wall boundary, a stepwise Dirichlet type boundary condition consisting of bilinear interpolations in both streamwise direction and time is implemented.

Furthermore, a uniform inlet velocity boundary condition is used. This boundary condition is preferred over the parabolic profile formerly used in [23], as the increased experimental thickness values close to the inlet suggest the existence of enhanced gradients in that region.

A summary of the specified boundary conditions is given in Table 4.

As previously explained, the TermoFluids code uses explicit time integration schemes for the momentum equation. Due to the fact that frost growth experiments usually range between 1 to 3 hours, the size of the mesh cells needs to be as large as possible while preserving the grid independence in order not

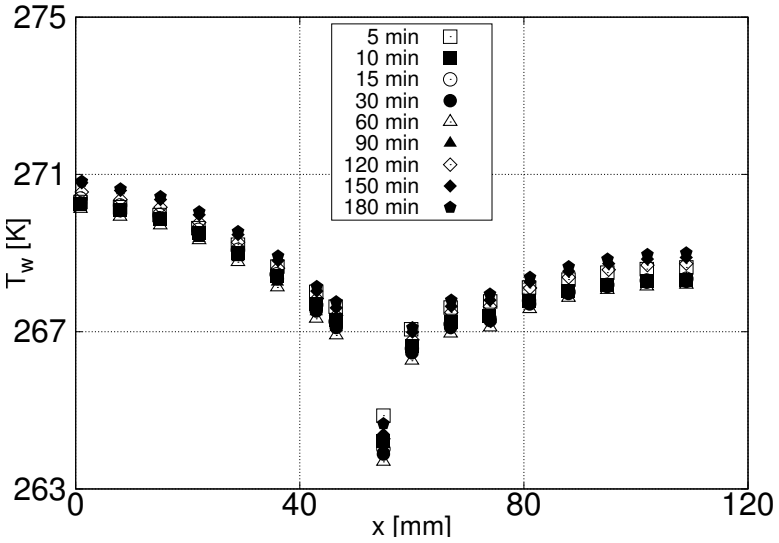

Figure 8: Experimental data aquired by Kwon *et al.* [28], and hereby used as a wall temperature boundary condition for the bottom wall.

Table 4: Boundary conditions

Side	v	p	ρ_v	ε_v	T
Bottom wall*	0	$\partial p/\partial n = 0$	$\partial \rho_v/\partial n = 0$	$\partial \varepsilon_v/\partial n = 0$	$T_W(x,t)^\dagger$
Upper wall	0	$\partial p/\partial n = 0$	$\partial \rho_v/\partial n = 0$	$\partial \varepsilon_v/\partial n = 0$	$\partial T/\partial n = 0$
Inlet	$v_{\mathrm{ha,in}}$	$\partial p/\partial n = 0$	$\rho_{v,\mathrm{in}}$	$\partial \varepsilon_v/\partial n = 0$	$T_{\mathrm{ha,in}}$
Outlet	$\partial v/\partial n = 0$	0	$\partial \rho_v/\partial n = 0$	$\partial \varepsilon_v/\partial n = 0$	$\partial T/\partial n = 0$

* Contains the special treatment explained in Sec.3.5.

† Bilinear interpolation of the experimental data, shown in Fig. 8.

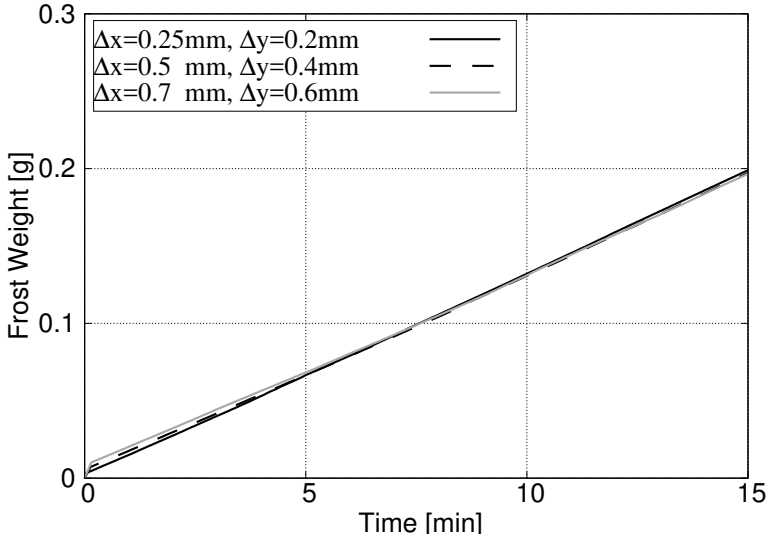

Figure 9: Grid independence study. The model parameters correspond to case `VP_high_Prag` defined in Table 5.

to reach too small time steps. Figure 9 shows a grid independence study with three different meshes with $\{\Delta x, \Delta y\}$-pairs of $\{0.25, 0.2\}$mm, $\{0.5, 0.4\}$mm and $\{0.7, 0.6\}$mm. The study shows good agreement of the accumulated frost among the three meshes. Furthermore, the mesh comparison carried out in [23] also showed that the rate of ice deposition is almost unchanged when changing from meshes with cell sizes of $\{1, 1\}$mm to $\{0.1, 0.1\}$mm. As a consequence, and recalling that the main purpose of the present study is to introduce and emphasize a new methodology capable to simulate the frost growth, the present 2D-study shows the results acquired with a uniform structured mesh of 220 x 10 cells, with $\Delta x = 0.5$mm and $\Delta y = 0.4$mm. The mesh size and the given numerical integration schemes (see Sec. 3) lead to time steps of the order of 10^{-4} to $10^{-5}s$. Speedup tests using different number of cores (1,2,4 and 8 cores of Intel Xeon processors, model E5-2683 v3) were carried out at the HPC cluster facilities of the Heat and Mass Transfer Technological Center. Results showed that the optimum was reached whenever using 4 cores, allowing the simulations to compute an average of 30 min per week. Ongoing work is focused on the optimization of the code and the implementation of fully implicit integration schemes, in order to diminish the computational effort of the simulations.

Furthermore, despite the fact that in [23], an extra 5 mm domain had been added to the inlet and outlet boundaries to avoid possible numerical instabilities as previously suggested by Wu *et al.* [21], the methodology hereby presented gives a stable solution close to the inflow and to the outflow, regardless of how close the boundary to the growing frost sheet is. Hence, the computed domain consists of 110 mm in the streamwise direction. Moreover, not accounting for the added domain close to the inlet as well as imposing uniform inflow boundary

Case	Momentum model	Ξ	$C_{\mathrm{VP,HC}}$	μ
`VP_high_Prag`	Voller and Prakash [27]	1	1.50e06	Prager *et al.* [31]
`VP_low_Prag`	Voller and Prakash [27]	1	6.05e03	Prager *et al.* [31]
`HC_high_Prag`	Hsu and Cheng [26]	ε_v	8.72e10	Prager *et al.* [31]
`HC_low_Prag`	Hsu and Cheng [26]	ε_v	7.03e08	Prager *et al.* [31]
`VP_low_Gall`	Voller and Prakash [27]	1	6.05e03	Le Gall *et al.* [17], F=5

Table 5: Tested numerical models.

conditions, allows to solve the enhanced gradients generated in that region, which produce larger frost growths (notice the experimental points measured at $x = 1$mm in Fig. 15).

5. Numerical tests

The dynamic mesh method presented in [19], which neglected the convection within the frost sheet, reported porosity values above 0.9 in approximately 80% of the frost layer thickness. In this method, an artificially enhanced diffusion resistance factor ($\mu > 1$) was needed in order to match the experiments, namely, Le Gall's correlation [17] with a factor F=5. Accurate results were found for the thickness profiles and the deposited mass. However, despite the aforementioned porosity distributions agreed with the numerical results obtained by Na and Webb [6], the resulting morphology of the frost layer remained unknown, as no such data is yet to be reported experimentally. Hence, the implementation of the fixed grid method was a motivation to give more clarity into two main aspects. First, whether the porosity distributions within the frost layer are similar to the ones obtained using the dynamic mesh method. And second, whether an enhanced diffusion resistance factor is still needed (as in the dynamic mesh method) if the convection within the frost layer is being accounted.

The numerical tests carried out in this study were designed both aiming to give answers to the former, which will be later discussed in Sec.5.2, as well as to study the behaviour of the presented model. A summary of the selected tests is shown in Table 5. In particular, the goal is to study:

- The differences between the two types of porous media treatment presented in Sec. 2, $\Xi = [1, \varepsilon_v]$, while maintaining the Darcian source terms as similar as possible, i.e. a C_{VP} and C_{HC} such that $S_{\mathrm{VP}} \approx S_{\mathrm{HC}}$.
- The impact of the velocity damping factor, directly related to the constant $C_{\mathrm{VP,HC}}$ of the Darcian source term.
- The effect of using artificially increased diffusion resistance factors.

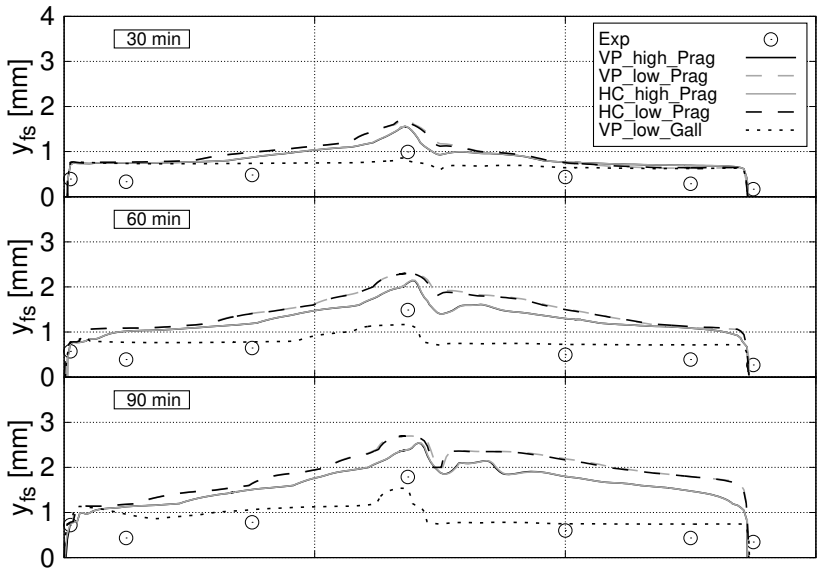

Figure 10: Frost thickness distributions given at $\varepsilon_v = 0.99$. Comparison with the experimental data acquired by Kwon *et al.* [28].

5.1. Results

The thickness distributions of the frost layer at different instants are shown in Fig. 10. Each distribution corresponds to each of the cases listed in Table 5. Due to the fact that using a static mesh does not allow a fully accurate tracking of the air-frost interface (the air-frost interface is located within the limits of the ice containing cells which have fully air containing cells neighbours), the thickness distributions shown in Fig. 10 correspond to contour plots at $\varepsilon_v = 0.99$. Note that using an $\varepsilon_v = 1$ contour condition would imply defining the frost-air interface at the very edges between ice containing cells and fully air containing cells, regardless the amount of deposited ice in the latter. Therefore, the frost layer surface was defined such that: first, the interface cells, although they are treated as frost-cells, they are not fully covered by frost. And second, the frost surface should not pass through inner frost cells, only interface cells. The fulfillment of these criteria was achieved by high porosity values, choosing $\varepsilon_v = 0.99$ as a representative number. In addition, the evolution of the accumulated frost weight at the lower boundary of the duct is shown in Fig.11. The experimental data gathered by Kwon *et al.* [28] is also depicted in both figures. The numerical tests are solved up to 90 min, as the authors find it a more than adequate elapsed time to represent the behaviour of the set up of each case. Results up to 180 min are also shown for case `VP_high_Prag`.

A comparison of the solutions of the porosity and temperature distributions, as well as the velocity field, of cases `VP_high_Prag`, `VP_low_Prag` and

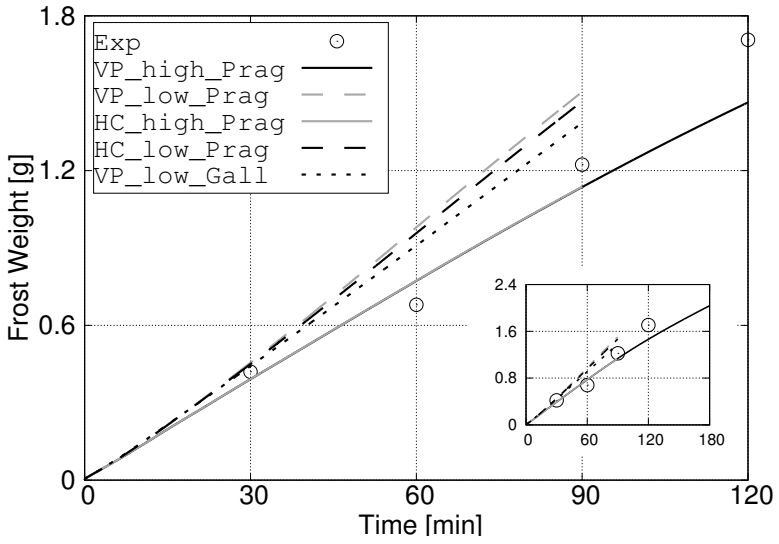

Figure 11: Frost weight evolution with time.

`VP_low_Gall` at 60 min is also provided in Figs.12, 13 and 14. Furthermore, the porosity distributions up to 180 min of case `VP_high_Prag` are depicted in Fig.15.

Solutions show almost no differences between the two types of porous media treatment given to the convective term of the momentum equation with large C-values (see that cases `VP_high_Prag` and `HC_high_Prag` appear overlapped in Figs. 10 and 11). Only very slight variations arise when using lower values of C (see cases `VP_low_Prag` and `HC_low_Prag` in Figs. 10 and 11), due to the fact that the expressions given in Eqs.15 and 16 move further apart as ε_v takes lower values (see Fig. 2). Therefore, the simplification of the porous media treatment put forward by Voller and Prakash [27] for mushy regions ($\Xi = 1$), in comparison with the one of Hsu and Cheng [26] ($\Xi = \varepsilon_v$), seems to give good enough approximations when solving the frost growth under the tested C-values.

Differences arise when using different values of the Darcian source term constant C. Lower C-values mean less resistance exerted by the frost layer on the air flow, which allows more water vapour to soak into it. As a consequence, larger deposition rates are found (e.g. note the slope differences between cases `VP_high_Prag` and `VP_low_Prag`, or cases `HC_high_Prag` and `HC_low_Prag`, shown in Fig. 11). Moreover, note that the corresponding thickness profiles given in Fig. 10 bring out that lower values of C not only let larger water vapour deposition, but also the fact that the densification along the duct is distributed differently (see Figs. 12a and 12b). Higher deposition rates are found in the upstream region ($x < 50$ mm), due to the fact that more vapour is penetrating the frost layer. Thus enlarging the drop of the bulk moisture in the first 60 mm

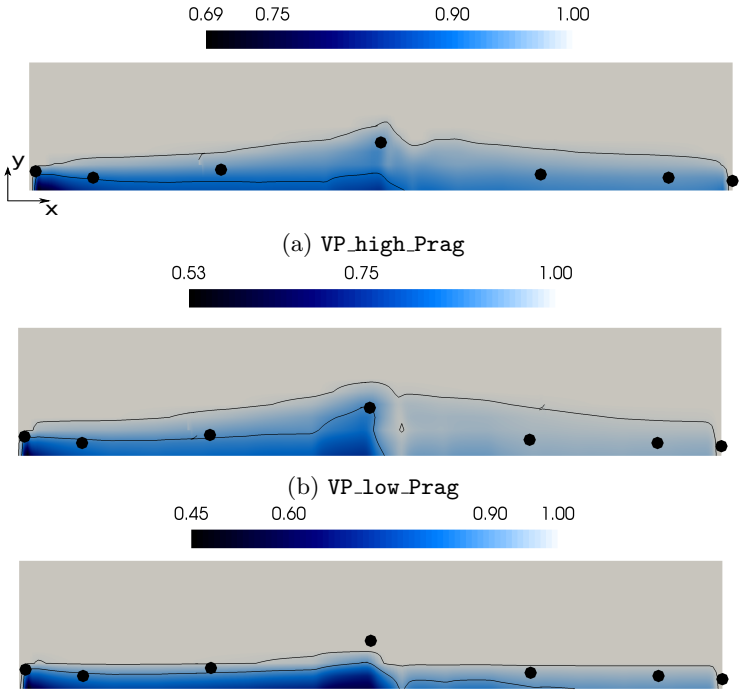

(a) `VP_high_Prag`

(b) `VP_low_Prag`

(c) `VP_low_Gall`

Figure 12: Porosity distributions, and contours of ε_v at 0.9 and 0.99 at 60 min. Circles correspond to the experimental frost thickness values [28]. The image scaling is x :1:5, y :1:1.

in the streamwise direction, which at the same time leads to a lower deposition in the downstream region ($x > 60$ mm) because of the reduced amount of the transported water vapour.

On the other hand, larger differences are found among the thickness distributions whenever using enhanced diffusion resistance factors (see cases `VP_low_Prag` and `VP_low_Gall` depicted in Figs. 10, 12b and 12c). The enhanced water vapour diffusivity allows a larger part of the vapour impinging the frost surface to diffuse into the frost sheet, which otherwise would remain in the cells close to the frost surface.

The porosity distributions shown in Figs.12 and 15 show that the densification occurs mainly close to the inlet, where higher gradients are located because of the uniform inflow boundary condition, as well as the central region, where lower wall temperatures are set. An increase of the porosity at certain locations in the downstream region (beginning at $x \approx 60$ mm) observed only in advanced states of case `VP_high_Prag`, starting from 120 min onwards in Fig.15, has also been noted. The origin of such effect, which might be numerical, is unclear. Further simulations using denser meshes might give an explanation to this situation.

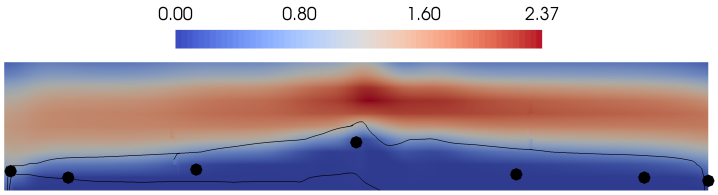

(a) `VP_high_Prag`

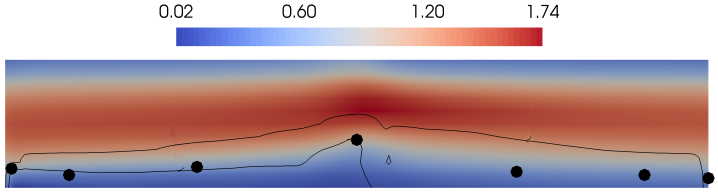

(b) `VP_low_Prag`

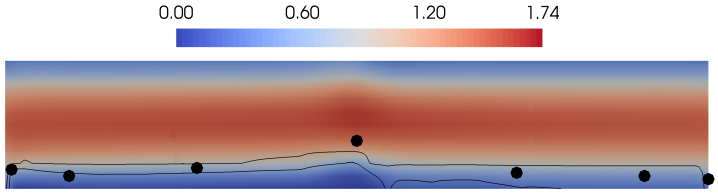

(c) `VP_low_Gall`

Figure 13: Velocity fields in m/s, and contours of ε_v at 0.9 and 0.99 at 60 min. Circles correspond to the experimental frost thickness values [28]. The image scaling is x :1:5, y :1:1.

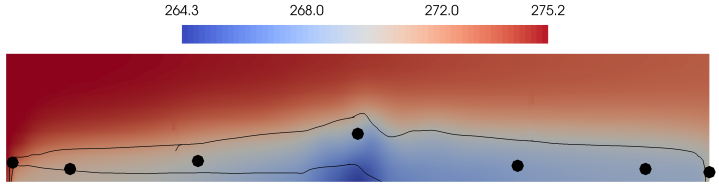

(a) `VP_high_Prag`

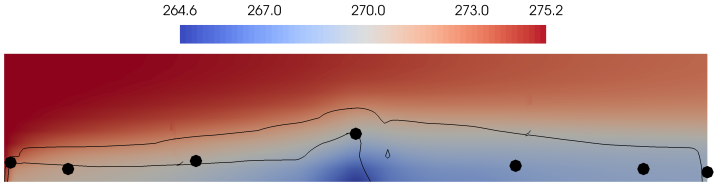

(b) `VP_low_Prag`

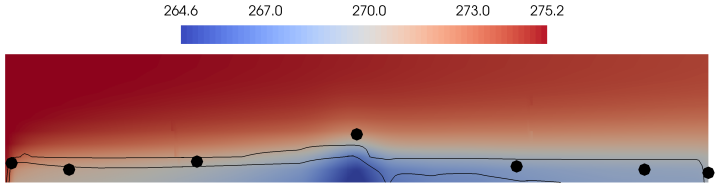

(c) `VP_low_Gall`

Figure 14: Temperature distributions in K, and contours of ε_v at 0.9 and 0.99 at 60 min. Circles correspond to the experimental frost thickness values [28]. The image scaling is x :1:5, y :1:1.

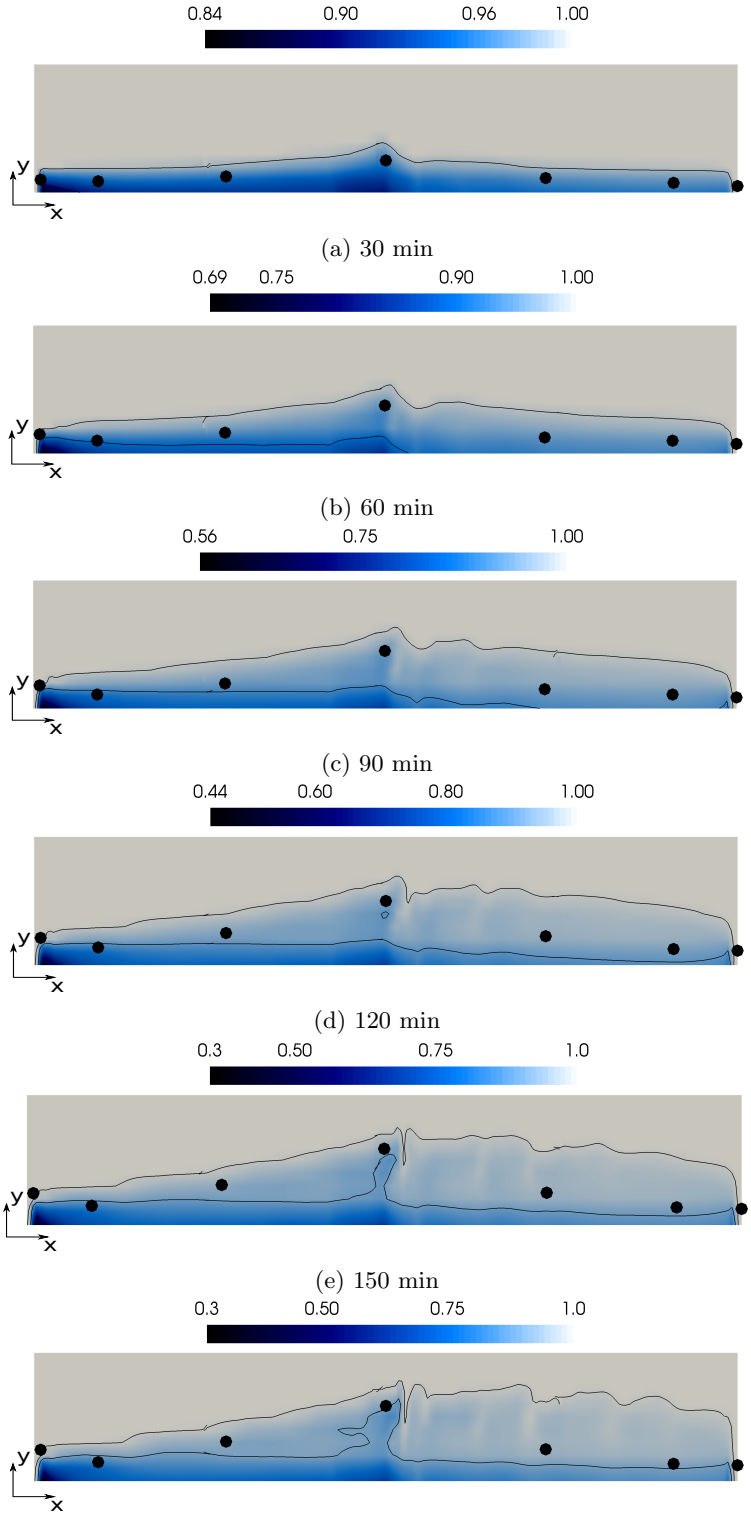

Figure 15: Porosity ditributions of `VP_high_Prag`. Contours of ε_v at 0.9 and 0.99. Circles correspond to the experimental frost thickness values [28]. The image scaling is x :1:5, y :1:1.

In addition, notice how the bulk temperature shown in Fig.14 decreases because of the contact with the lower boundary, as well as how the increased thermal conductivity within the frost sheet allows the cold temperatures to propagate throughout the layer.

The velocity fields shown in Fig.13 indicate that convection within the range $\varepsilon_v \in [0.9-0.99]$ becomes less important when increasing the value of the constant C, as seen by the close to zero velocity values observed in that region. Indeed, the larger the C-value is, the bigger is the region with high porosity values, a fact that agrees qualitatively to the solutions without convection obtained in [19].

5.2. Discussion

Despite the fact that using non-artificially increased diffusion resistance factors, i.e. Prager's correlation, lead to overall overpredicted growths (see Fig.10), it has been verified that the value of the constant C regulates the local densification. It is observed that the low C-values tested induce larger densifications in the upstream region ($x < 50$ mm), allowing a lower amount of water vapour to deposit on the downstream region ($x > 60$ mm). On the contrary, the large C-values tested allow a more homogeneous deposition of water vapour. Thus, keeping a larger amount in the dowstream region, which translates into higher growths. Regardless of the shifted solution of the air-frost interface when using Prager's diffusivity, the thickness distributions obtained when using the low C-values agree better to the experimental data. Recall that despite the fact that we are using a constant value for C, it could have a dependance on the particle diameter, as for example, $\sim 1/d_p^2$, as given in Eq. 16. In more porous regions (i.e. close to the frost-air surface), one should expect lower values of d_p. The lack of such data within the frost layer highlights the actual need to perform experiments aiming to study the internal morphology.

On the other hand, it has been observed that the usage of artificially increased diffusion resistance factors (Le Gall *et al.* [17] with an F factor of 5) promote the densification of the frost layer in exchange of its growth. The solution of case `VP_low_Gall` underpredicts the growth. Hence, given the tested mesh, one should expect better agreements when using lower values of F.

As a conclusion, the source term of the momentum equation regulates, in a way, where the densification will be held, as well as the shape of the air-frost interface. Whereas enhancing the diffusion resistance factor regulates the rate of growth. It seems that enhanced diffusion resistance factors are needed to match the experimental data, although with smaller enhancements than the ones used in [19], which would prove that the convective effects play a role within the frost layer. However, despite convection should be included in the model, the need of using a $\mu > 1$ means that the latter is not accounting for other physical effects which are taking place within the frost layer (see [17, 37, 19]).

6. Conclusions

The presented model accounts for the appearance, growth and densification of frost. The model is based on a finite volume approach which uses a fixed grid. A single set of equations is set both for the free air and the frost layer, where the thermophysical properties are dynamically adapted for each region and where phase changes are triggered by the thermophysical state of the cells.

The capabilities of the numerical model have been tested in a channel flow with a non-homogeneously cooled lower boundary, previously studied experimentally by Kwon *et al.* [28]. In particular, the studied parameters include the porosity model used to calculate the convection outside and within the frost layer, the magnitude of the Darcian coefficient, which causes the damping of the velocity field within the porous medium, and the enhancement of the diffusion resistance factors.

Results show that using Darcian coefficient values such that convection is allowed at the high porosity regions ($\varepsilon_v > 0.9$), imply larger local densifications of the frost sheet in the upstream region, accompanied by a decrease on the vapour deposition in the downstream region. Moreover, it has been verified that whenever allowing convection within the frost layer, the artificial enhancement of the diffusion resistance factor needs to be reduced compared to a case where no convection is allowed [19], a fact that confirms the idea that convective effects play a significant role in high porosity regions. Further simulations using denser meshes should be carried out to find the best combination of the input parameters of the model, i.e. the frost layer conductivity, the diffusion resistance factor, and the momentum source term coefficient, in order to provide more accurate predictions of the phenomenon.

Notwithstanding the fact that one could set up a numerical model able to reproduce the growth of the frost layer by optimizing the empirical and numerical inputs, it is essential to further encourage experimental research to tackle the internal processes of frost sheets. Specifically, from a macroscopical point of view, the ones related to the effective diffusivity and the particle diameter dependency of the Darcian coefficient.

7. Conflict of interest

None declared.

Acknowledgments

This work has been financially supported by the Research and University Secretary, Department of Business and Knowledge of the Generalitat de Catalunya (2015 DI 0069).

The authors would like to thank the Universidad de la República, Uruguay, for its financial support through the mobility program "720-Contrapartida de Convenios".

The authors would also like to acknowledge Dr. Nikos Nikiforakis and the members of the Laboratory for Scientific Computing (Department of Physics, University of Cambridge), and Dr. Sean Lovett (Schlumberger Cambridge Research), for the ideas put forward and the productive discussions on this research topic.

References

[1] Olivier Parent and Adrian Ilinca. Anti-icing and de-icing techniques for wind turbines: Critical review. *Cold regions science and technology*, 65(1):88–96, 2011.

[2] Kripa K Varanasi, Tao Deng, J David Smith, Ming Hsu, and Nitin Bhate. Frost formation and ice adhesion on superhydrophobic surfaces. *Applied Physics Letters*, 97(23):234102, 2010.

[3] Saurabh Nath, S Farzad Ahmadi, and Jonathan B Boreyko. A review of condensation frosting. *Nanoscale and Microscale Thermophysical Engineering*, 21(2):81–101, 2017.

[4] Kwan-Soo Lee, Sung Jhee, and Dong-Keun Yang. Prediction of the frost formation on a cold flat surface. *International Journal of Heat and Mass Transfer*, 46(20):3789–96, September 2003.

[5] Y.B. Lee and S.T. Ro. Analysis of the frost growth on a flat plate by simple models of saturation and supersaturation. *Experimental Thermal and Fluid Science*, 29(6):685–96, July 2005.

[6] Byeongchul Na and Ralph L. Webb. New model for frost growth rate. *International Journal of Heat and Mass Transfer*, 47:925–36, 2004.

[7] Christian JL Hermes, Robson O Piucco, Jader R Barbosa, and Cláudio Melo. A study of frost growth and densification on flat surfaces. *Experimental Thermal and Fluid Science*, 33(2):371–379, 2009.

[8] Amne El Cheikh and Anthony Jacobi. A mathematical model for frost growth and densification on flat surfaces. *International Journal of Heat and Mass Transfer*, 77:604–11, 2014.

[9] Max Kandula. Frost growth and densification in laminar flow over flat surfaces. *International Journal of Heat and Mass Transfer*, 54:3719–31, 2011.

[10] Donghee Kim, Chiwon Kim, and Kwan-Soo Lee. Frosting model for predicting macroscopic and local frost behaviors on a cold plate. *International Journal of Heat and Mass Transfer*, 82:135–142, 2015.

[11] Bernard Frankovic Kristian Lenic, Anica Trp. Transient two-dimensional model of frost formation on a fin-and-tube heat exchanger. *International Journal of Heat and Mass Transfer*, 52:22–32, 2009.

[12] JM Armengol, CT Salinas, J Xaman, and KAR Ismail. Modeling of frost formation over parallel cold plates considering a two-dimensional growth rate. *International Journal of Thermal Sciences*, 104:245–256, 2016.

[13] Chiwon Kim, Jaehwan Lee, and Kwan-Soo Lee. Numerical modeling of frost growth and densification on a cold plate using frost formation resistance. *International Journal of Heat and Mass Transfer*, 115:1055–1063, 2017.

[14] Jaehwan Lee, Junghan Kim, Dong Rip Kim, and Kwan-Soo Lee. Modeling of frost layer growth considering frost porosity. *International Journal of Heat and Mass Transfer*, 126:980–988, 2018.

[15] B.W. Jones and J.D. Parker. Frost formation with varying environmental parameters. *Journal of Heat Transfer*, 97(2):255–259, 1975.

[16] Y.-X. Tao, R.W. Besant, and K.S. Rezkallah. A mathematical model for predicting the densification and growth of frost on a flat plate. *International Journal of Heat and Mass Transfer*, 36(2):353–63, 1993.

[17] R. Le Gall, J.M. Grillot, and C. Jallut. Modelling of frost growth and densification. *International Journal of Heat and Mass Transfer*, 40(13):3177–87, 1997.

[18] Simon Ellgas and Michael Pfitzner. Modeling frost formation within a commercial 3-d cfd code. *Numerical Heat Transfer, Part A: Applications*, 53(5):485–506, 2007.

[19] Eduard Bartrons, Carles Oliet, Enrique Gutirrez, Alireza Naseri, and Carlos David Prez-Segarra. A finite volume method to solve the frost growth using dynamic meshes. *International Journal of Heat and Mass Transfer*, 124:615–628, 2018.

[20] J Cui, WZ Li, Y Liu, and ZY Jiang. A new time- and space-dependent model for predicting frost formation. *Applied Thermal Engineering*, 31:447–457, 2011.

[21] Xiaomin Wu, Qiang Ma, Fuqiang Chu, and Shan Hu. Phase change mass transfer model for frost growth and densification. *International Journal of Heat and Mass Transfer*, 96:11–19, 2016.

[22] Xiaomin Wu, Fuqiang Chu, and Qiang Ma. Frosting model based on phase change driving force. *International Journal of Heat and Mass Transfer*, 110:760–767, 2017.

[23] Eduard Bartrons, PA Galione, Giorgos Papakokkinos, and Carles D Pérez-Segarra. Fixed-grid numerical modeling of frost formation. In *23rd AIAA Computational Fluid Dynamics Conference*, page 4505, 2017.

[24] PA Galione, O Lehmkuhl, J Rigola, and A Oliva. Fixed-grid modeling of solid-liquid phase change in unstructured meshes using explicit time schemes. *Numerical Heat Transfer, Part B: Fundamentals*, 65(1):27–52, 2014.

[25] PA Galione, O Lehmkuhl, J Rigola, and A Oliva. Fixed-grid numerical modeling of melting and solidification using variable thermo-physical properties–application to the melting of n-octadecane inside a spherical capsule. *International Journal of Heat and Mass Transfer*, 86:721–743, 2015.

[26] CT Hsu and P Cheng. Thermal dispersion in a porous medium. *International Journal of Heat and Mass Transfer*, 33(8):1587–1597, 1990.

[27] Vaughan R Voller and C Prakash. A fixed grid numerical modelling methodology for convection-diffusion mushy region phase-change problems. *International Journal of Heat and Mass Transfer*, 30(8):1709–1719, 1987.

[28] Jeong-Tae Kwon, Hyo Jae Lim, Young-Chul Kwon, Shigeru Koyama, Dong-Hwi Kim, and Chieko Kondou. An experimental study on frosting of laminar air flow on a cold surface with local cooling. *International Journal of Refrigeration*, 29(5):754–760, 2006.

[29] E Bartrons, CD Perez-Segarra, and C Oliet. Frost formation: Optimizing solutions under a finite volume approach. In *Journal of Physics: Conference Series*, volume 745, page 032062. IOP Publishing, 2016.

[30] H Auracher. Water vapour diffusion and frost formation in capillaries. In *Bulletin of the International Institute of Refrigeration*, pages 477–88, 1972.

[31] R.E. Cunningham and R.J.J. Williams. *Diffusion in Gases and Porous Media*. New York: Plenum Press, 1980.

[32] T. E. Fessler. *WETAIR - a computer code for calculating thermodynamic and transport properties of air-water mixtures*, volume Tech. Report 1466. NASA, 1979.

[33] Termo fluids s.l., webpage: www.termofluids.com.

[34] J. Muela. *Modelling and numerical simulation of combustion and multiphase flows using finite volume methods on unstructured meshes*. PhD thesis, Polytechnic University of Catalonia, 2018.

[35] Jean-Luc Guermond, Peter Minev, and Jie Shen. An overview of projection methods for incompressible flows. *Computer methods in applied mechanics and engineering*, 195(44):6011–6045, 2006.

[36] *ASHRAE Handbook Fundamentals*. American Society of Heating, Refrigerating and Air-conditioning Engineers, Inc., si edition edition, 2009.

[37] Z. Yosida. Physical studies on deposited snow. i: Thermal properties. *Contributions from the Institute of Low Temperature Science*, 7(7):19–74, 1955.